Journal of Materials Chemistry A

Ultrafast Preparation of Ruthenium Nanoparticle/Molybdenum Oxide/Nitrogen-Doped Carbon Nanocomposites by Magnetic Induction Heating for Efficient Hydrogen Evolution Reaction

Journal:	*Journal of Materials Chemistry A*
Manuscript ID	TA-ART-02-2024-000884.R1
Article Type:	Paper
Date Submitted by the Author:	30-Apr-2024

Complete List of Authors:	Yu, Bingzhe; University of California Santa Cruz, ; \ Liu, Qiming; University of California Santa Cruz, Chemistry and Biochemistry Pan, Dingjie; University of California Santa Cruz, Chemistry and Biochemistry Singewald, Kevin; University of California Santa Cruz, Chemistry and Biochemistry DuBois, Davida; University of California Santa Cruz, Chemistry Tressel, John; University of California Santa Cruz, Chemistry and Biochemistry Hou, Bryan; University of California Santa Cruz, Chemistry and Biochemistry Millhauser, Glenn; University of California Santa Cruz, Chemistry and Biochemistry Bridges, Frank; University of California Santa Cruz, Physics Department Chen, Shaowei; University of California Santa Cruz, Department of Chemistry and Biochemistry

Ultrafast preparation of ruthenium nanoparticle/molybdenum oxide/nitrogen-doped carbon nanocomposites by magnetic induction heating for efficient hydrogen evolution reaction

Bingzhe Yu,[a] Qiming Liu,[a] Dingjie Pan,[a] Kevin Singewald,[a] Davida DuBois,[a] John Tressel,[a] Bryan Hou,[a] Glenn L. Millhauser,[a] Frank Bridges,[b] and Shaowei Chen[a,]*

[a] Department of Chemistry and Biochemistry, University of California, 1156 High Street, Santa Cruz, CA 95064, United States

[b] Department of Physics, University of California, 1156 High Street, Santa Cruz, CA 95064, United States

* E-mail: shaowei@ucsc.edu

Abstract Ruthenium has emerged as a viable electrocatalyst towards hydrogen evolution reaction (HER) in alkaline media, where the performance can be further enhanced by slight weakening of H adsorption. Herein, nanocomposites with ruthenium nanoparticles dispersed on molybdenum oxide supported on nitrogen-doped carbon are synthesized via ultrafast magnetic induction heating at controlled currents for only 10 s, and exhibit evident HER activity in 1 M KOH. Among the series, the $RuMoO_x$/NC-5 sample, with a Ru:Mo atomic ratio of ca. 3:1, shows the best performance, featuring a low overpotential of only -39 mV to reach the current density of 10 mA cm^{-2} and a low Tafel slope of 28.3 mV dec^{-1}, which is markedly better than those of the monometal counterparts, samples with a lower Ru:Mo ratio, and even commercial 20 wt% Pt/C. This is attributed to weakened H adsorption on Ru active sites by the synergetic interactions between

ruthenium and molybdenum oxide, as confirmed in theoretical studies based on density functional theory calculations.

Keywords: $RuMoO_x$ composite; electron transfer; magnetic induction heating; hydrogen evolution reaction; density functional theory

Introduction

With the rapid depletion of fossil fuels, development of green and sustainable energy technologies has been attracting extensive interest.[1] Hydrogen (H_2) represents a unique source of energy due to its high energy density, zero-carbon emission, and environmental cleanliness.[2] Currently, hydrogen is produced predominantly by coal gasification or steam methane reforming, which is energy-intensive and emits a large amount of carbon dioxide, and the obtained hydrogen is generally known as grey hydrogen.[3] To move away from grey hydrogen to green hydrogen, one effective technology is based on electrochemical water splitting, which entails hydrogen evolution reaction (HER) at the cathode and oxygen evolution reaction (OER) at the anode.[4] Thanks to the complex reaction pathways and sluggish electron-transfer kinetics, appropriate catalysts are needed for both half-reactions such that a sufficiently high current density can be produced for practical applications. Currently platinum-based materials have been the catalysts of choice for HER.[5] However, the high cost and natural scarcity of Pt has hindered their widespread applications.[6] Ruthenium (Ru) has emerged as a promising alternative for HER electrocatalysis, in particular in alkaline media, thanks to its low energy barrier of water dissociation, comparable H adsorption to that of Pt, and only half of the cost of Pt (ca. \$450 vs \$950 per ounce).[7, 8] Nevertheless, as Ru resides on the left side of the HER volcano plot, the HER performance can be further enhanced by somewhat weakening the H adsorption.[7, 9] This can be achieved by dispersing ruthenium onto a functional scaffold, such as carbon, metal, and metal oxides.[10-12] For instance, Pi et al.[13] anchored subnanometer-sized Ru clusters on tungsten oxide nanowires by hydrothermal synthesis and observed a low overpotential (η_{10}) of −21 mV to reach the current density of 10 mA cm^{-2} in acidic media, which was ascribed to electrons transfer from Ru clusters to $W_{18}O_{49}$. In another study, Guo et al.[14] prepared Ru/CoO hybrids by thermal annealing and observed a high HER activity (η_{10} = −55 mV) in alkaline media, due to extensive oxygen vacancies in the oxide scaffold that facilitated water dissociation and enhanced the electrical conductivity. Naseeb et al.[15] synthesized Ru-CoO heterostructured nanoparticles and observed a low η_{10} of -90 mV in 1 M KOH, which was attributed to charge transfer from

Ru to CoO. Molybdenum oxides have also been used as a supporting matrix, as demonstrated by Liu et al.,[16] where MoRu diatomic pairs were dispersed on well-coupled graphene and MoO_{3-x} via controlled pyrolysis. The low η_{10} of -20 mV in 1 M KOH was ascribed to the abundant O and Ru vacancies on the composite surfaces. In another study, Yuan et al.[17] prepared Ru-MoO_2/C nanocomposites via two-stage calcination, and observed an extraordinary HER activity (η_{10} = −12 mV) in alkaline media, due to the formation oxygen vacancies and defective Ru sites.

In these earlier studies, the samples were mostly prepared by conventional pyrolysis that is energy- and time-consuming. Recently, magnetic induction heating (MIH) has been exploited as a powerful tool for ultrafast preparation of a range of functional nanocomposites for HER and OER electrocatalysis due to rapid Joule's heating within seconds,[18] such as FeNi spinel oxides,[19] Co nanoparticles encapsulated in defective carbon,[20] $RuCl_x$-decorated Ru nanoparticles,[10] and amorphous MoS_x nanocomposites.[21] In the present study, we prepared a series of nanocomposites using MIH at controlled currents for only 10 s where Ru nanoparticles were dispersed on molybdenum oxides (MoO_x) supported on N-doped carbon that was pyrolytically derived from zeolitic imidazolate framework-8 (ZIF-8). The resultant $RuMoO_x$/NC nanocomposites were found to possess a rather consistent Ru and Mo combined content of 3 to 4 at%. Electrochemical measurements showed that the $RuMoO_x$/NC composites exhibited a marked increase of the HER activity with a decreasing Mo:Ru atomic ratio, and the best sample $RuMoO_x$/NC-5 displayed a low η_{10} of -39 mV, a Tafel slope of 28.3 mV dec^{-1}, as well as excellent stability and durability in alkaline media. Such a performance was drastically better than those of the monometal counterparts of Ru/NC and MoO_x/NC, as well as commercial Pt/C. This was ascribed to electron transfer from Ru to the molybdenum oxide scaffold that weakened H adsorption on Ru, as evidenced by the results from density functional theory (DFT) calculations.

Result and discussion

The preparation of the $RuMoO_x$/NC nanocomposites consists of three major steps (**Figure 1a)**. First, N-doped carbon (NC) was synthesized by pyrolysis of ZIF-8 in a tube furnace at 900 ˚C for 3 h. Second, a controlled amount of $RuCl_3$ and $(NH_4)_6Mo_7O_{24}$ was loaded onto the N-doped carbon via freeze-drying, where the Mo:Ru molar feed ratio was set at 4:1, 2:1, 1:1, 1:2 and 1:4 with the total metal content kept roughly constant at 20 wt% of the carbon scaffold. Finally, the precursors were transformed to $RuMoO_x$/NC nanocomposites by MIH treatment at 300 A for 10 s (**Figure 1b**), which were referred to as $RuMoO_x$/NC-n

(n = 1, 2, 3, 4, and 5). Two control samples were prepared in the same manner except for the addition of $RuCl_3$ or $(NH_4)_6Mo_7O_{24}$ before freeze-drying, and denoted as MoO_x/NC and Ru/NC, respectively. This is to take advantage of the Joule's heating effect that can produce a temperature over 1000 °C within seconds (**Figure 1c**).[10, 19-21] The details are included in the Experimental Section.

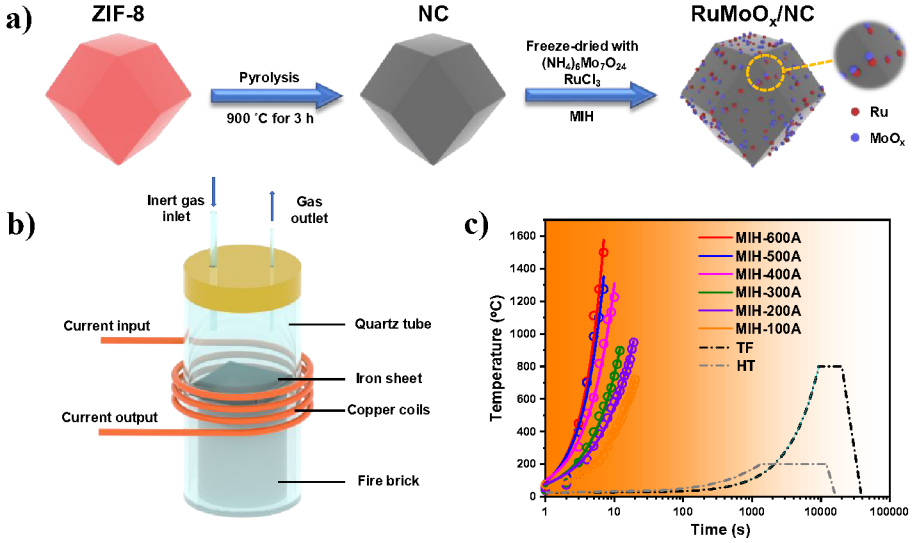

Figure 1. Schematic illustrations of (a) ultrafast synthesis of $RuMoO_x$/NC by (b) MIH. (c) Heating temperature as a function of MIH time at varied currents, as determined with an infrared thermometer. TF and HT denote conventional tube furnace and hydrothermal method, respectively.[10, 19-21]

The sample structures were first examined by scanning electron microscopy (SEM) and transmission electron microscopy (TEM) measurements. From the SEM images in **Figure 2a-b**, it can be seen that $RuMoO_x$/NC-5 retained the dodecahedral morphology of the original ZIF-8 precursor, with a lateral size of ca. 315 nm. In TEM measurements (**Figure 2c**), the sample can be seen to consist of a number of dark-contrast nanoparticles embedded onto a low-contrast matrix; and high-resolution TEM measurements showed that the nanoparticles possess well-defined lattice fringes with an interplanar spacing of 0.237 nm (**Figure 2d-e**), which is consistent with the (100) planes of metallic Ru (PDF 06-0663),[22, 23] indicating the formation of Ru nanoparticles, likely due to thermal reduction of $RuCl_3$ to metallic Ru by carbon at elevated temperatures.[10] The corresponding core size histogram is shown in **Figure 2f**, where the nanoparticles can be seen to fall primarily within the range of 1 to 5 nm, with an average diameter of 2.85 ± 0.91 nm.

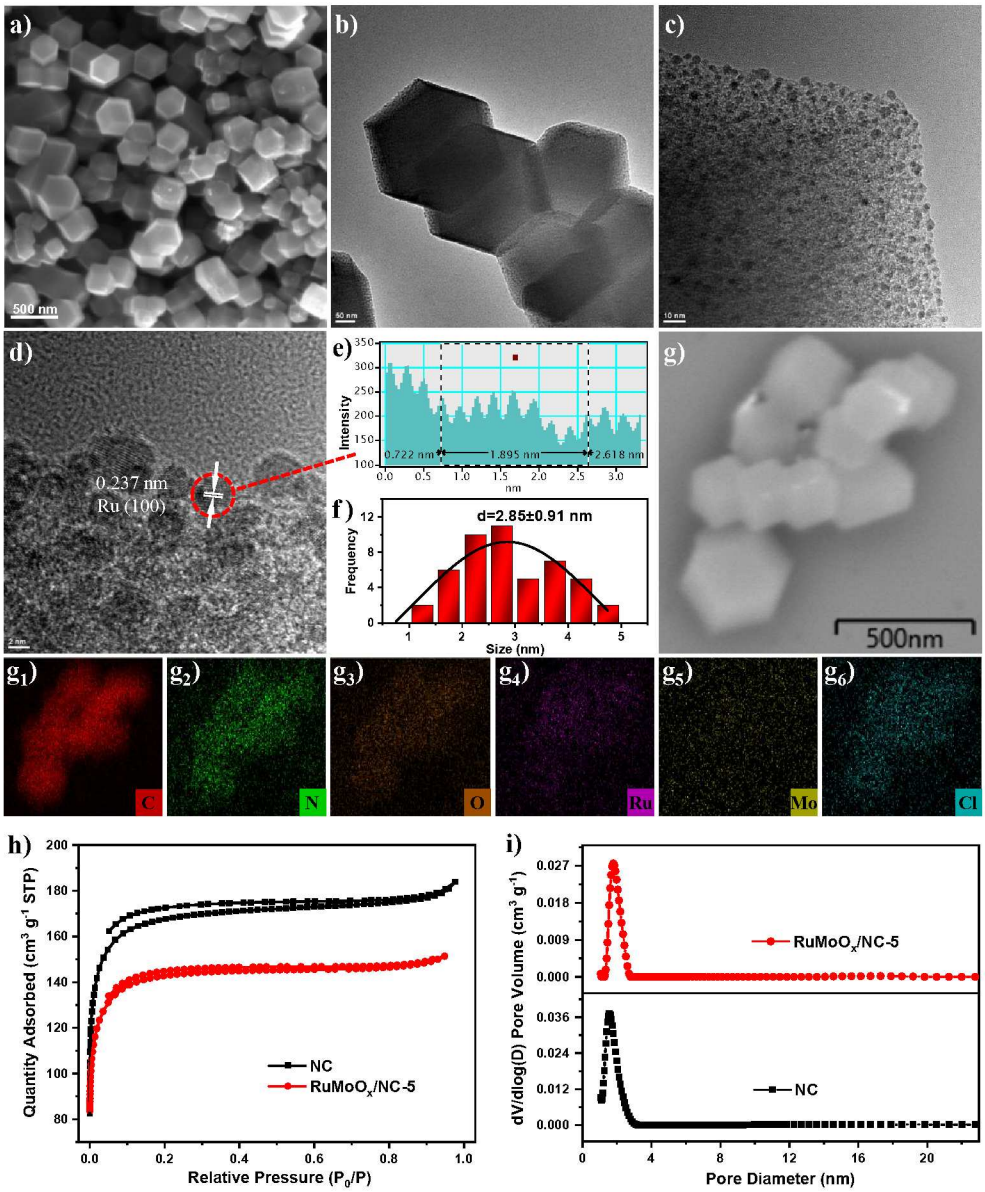

Figure 2. (a) SEM image and (b, c, d) TEM images of $RuMoO_x$/NC-5. (e) Interplanar spacing of the lattice fringes of the circled area in (d). (f) Particle size distribution histogram based on panel (b). (g) SEM image and elemental maps of (g_1) C, (g_2) N, (g_3) O, (g_4) Ru, (g_5) Mo and (g_6) Cl. Scale bars are (a) 500 nm, (b) 50, (c) 10, (d) 2, and (g) 500 nm. (h) Nitrogen adsorption-desorption isotherms and (i) pore size distribution profiles of NC and $RuMoO_x$/NC-5.

The morphological features were similar with other samples in the series (**Figure S1-S6**). Nevertheless, for the two samples prepared at a high Mo:Ru feed ratio (i.e., $RuMoO_x$/NC-2 and $RuMoO_x$/NC-1), no nanoparticles could be resolved; instead, the samples exhibited two interplanar spacings of 0.348 and 0.384 nm (**Figure S2b and S3b)**, consistent with the (210) and (001) planes of MoO_3 (PDF 21-

0569 and 47-1081), suggesting the successful conversion of $(NH_4)_6Mo_7O_{24}$ to MoO_3.[24, 25] In addition, one can see that the Ru nanoparticle size diminished markedly with the decreasing initial feed of $RuCl_3$ in sample preparation (**Figures S7)**, 10.99 ± 3.14 nm for Ru/NC, 2.85 ± 0.91 nm for $RuMoO_x$/NC-5, 2.84 ± 0.57 nm for $RuMoO_x$/NC-4 and 1.99 ± 0.35 nm for $RuMoO_x$/NC-3. This suggests that the produced molybdenum oxide scaffold facilitated the dispersion of the ruthenium nanoparticles and impeded their agglomeration.

In elemental mapping analysis based on energy-dispersive X-ray spectroscopy (EDS) measurements (**Figure 2g**), the elements of C, N, O, Ru, Mo and Cl can be clearly resolved with a rather homogeneous distribution across the sample, suggesting good dispersion of Ru nanoparticles within the MoO_x/NC matrix and the nanocomposites were most likely functionalized with Cl residues. Consistent results were obtained for other samples in the series (**Figure S8-S14**) and the corresponding elemental compositions are listed in **Table S1**, where the total metal content was rather consistent at 3 to 4 at% within the series of samples, with an apparent decrease of the Mo:Ru atomic ratio from $RuMoO_x$/NC-1 to $RuMoO_x$/NC-5. Nevertheless, one can see that the Mo:Ru atomic ratio was greater than the initial feed ratio, most likely due to the higher thermal volatility of $RuCl_3$ than that of $(NH_4)_6Mo_7O_{24}$.

The porosity and specific surface areas of the samples were then examined by nitrogen sorption measurements. From **Figure 2h**, one can see that NC and $RuMoO_x$/NC-5 both exhibited a Type I isotherm, suggesting the formation of mostly micropores. In fact, from the pore size distributions in **Figure 2i**, one can see that the pores were under 2 nm for both NC and $RuMoO_x$/NC-5, averaging 1.56 nm for the former and 1.79 nm for the latter. Furthermore, the specific surface area can be seen to decrease slightly from 442.29 $m^2\ g^{-1}$ for NC to 382.51 $m^2\ g^{-1}$ for $RuMoO_x$/NC-5, likely due to the impregnation of $RuMoO_x$ into the NC pores.[26]

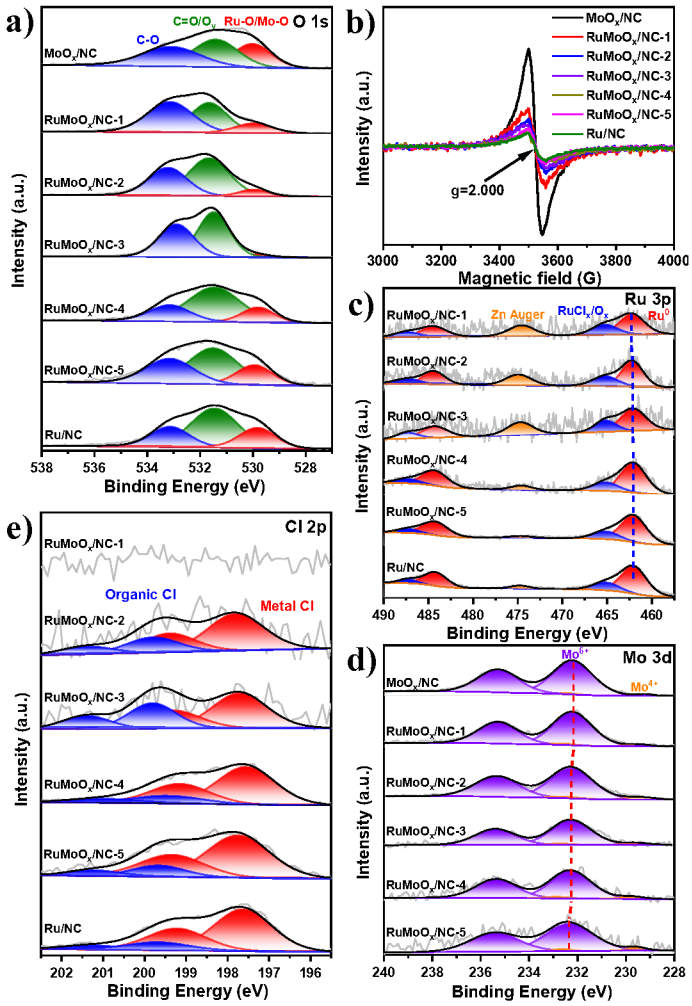

Figure 3. High-resolution XPS spectra of the (a) O 1s, (c) Ru 3p, (d) Mo 3d, and (e) Cl 2p electrons of the sample series, and (b) the corresponding EPR spectra.

The elemental composition and valency were then examined by X-ray photoelectron spectroscopy (XPS) measurements. **Figure S15** shows the survey spectra of the series of samples, where the O 1s, Mo 3s, Ru 3p, N 1s, C 1s, Cl 2s, Mo 3d and Cl 2p electrons can be readily resolved at ca. 532, 498, 461, 399, 285, 269, 232 and 198 eV, respectively (except that no Ru signals in MoO_x/NC and no Mo signals in Ru/NC). The corresponding elemental contents are listed in **Table S2** and **S3**. It can be seen that the Ru content increases, whereas the Mo content decreases, from $RuMoO_x$/NC-1 to $RuMoO_x$/NC-5, largely consistent with results from EDS analysis (**Table S1**).

The high-resolution scans of the C 1s electrons are shown in **Figure S16a**. Deconvolution yields three peaks at ca. 284.6, 286.3 and 288.5 eV, which can be attributed to the C-C, C-O-C and C=O species

of the N-doped carbon matrix.[27, 28] In addition, for samples with a high Ru content such as $RuMoO_x$/NC-4, $RuMoO_x$/NC-5 and Ru/NC, a doublet can be resolved at ca. 280.4 and 284.5 eV due to the $3d_{5/2}$ and $3d_{3/2}$ electrons of metallic Ru, and a minor one at a somewhat higher binding energy of 282.0 and 286.1 eV arising from $Ru^{\delta+}$ species.[10, 29, 30] The corresponding N 1s spectra are shown in **Figure S16b**, where three species can be resolved at 398.4 eV for pyridinic N, 400.1 eV for pyrrolic N and 401.2 eV for graphitic N, confirming the successful formation of N-doped carbon from ZIF-8.[31, 32] **Figure 3a** show the corresponding O 1s spectra, where the Ru-O/Mo-O peak can be resolved at ca. 529.9 eV, along with C=O and/or oxygen vacancy in MoO_x at 531.6 eV and C-O at 533.2 eV.[33-35] In fact, in EPR measurements (**Figure 3b)**, the samples can all be seen to display a symmetric profile centered at ca. 3524 G with a corresponding *g* value of 2.000, due to the formation of oxygen vacancies, which became intensified with increasing Mo loading.[17, 36] This suggests that the oxygen vacancies were formed primarily within the MoO_x scaffold.

The corresponding Ru 3p spectra are shown in **Figure 3c**, which consist of a dominant doublet at 462.2/484.3 eV that can be ascribed to the $3p_{3/2}/3p_{1/2}$ electrons of metallic Ru and a minor one at 465.1/487.3 eV to $Ru^{\delta+}$ (the peak at ca. 474.7 eV likely due to the Auger peak of residual Zn), in good agreement with results from the 3d spectra in **Figure S16a**.[37] Notably, in comparison to the monometal Ru/NC, the Ru 3p binding energies exhibited an apparent blue shift upon the incorporation of MoO_x into the composites, and increased with an increasing Mo loading (from $RuMoO_x$/NC-5 to $RuMoO_x$/NC-1), suggesting Ru to Mo electron transfer and hence increasingly electron-deficient Ru in the $RuMoO_x$/NC nanocomposites. For instance, the Ru 3p binding energies of $RuMoO_x$/NC-1 were the highest among the series, ca. 0.18 eV higher than those of Ru/NC (**Table S4**). The corresponding Mo 3d spectra are shown in **Figure 3d**, where deconvolution yields a major doublet at 232.2/235.3 eV for the $3d_{5/2}/3d_{3/2}$ electrons of Mo^{6+}, and a minor one at 229.5/232.6 eV for Mo^{4+}, suggesting the formation of MoO_x in the nanocomposites.[38, 39] Notably, a slight increase of the binding energies can be observed from $RuMoO_x$/NC-1 to $RuMoO_x$/NC-5, with $RuMoO_x$/NC-5 displaying the highest binding energies, ca. 0.14 eV greater than those of MoO_x/NC (**Table S5**), consistent with the diminishing content of oxygen vacancies as observed in the above EPR measurements (**Figure 3b**).

The Cl 2p spectra are shown in **Figure 3e**, where two doublets can be deconvoluted at 197.7/199.4 eV and 199.7/201.4 eV due to metal-Cl and organic Cl species, respectively.[40] The former suggests the formation of residual Cl species within the nanocomposites, most likely due to the incomplete decomposition of $RuCl_3$ during the ultrafast MIH treatment.[10] In fact, in EDS measurements (**Figure S8-S14**), the Cl content

can be seen to increase markedly from $RuMoO_x$/NC-1 to $RuMoO_x$/NC-5 (not detectable in MoO_x/NC) (**Table S1**).

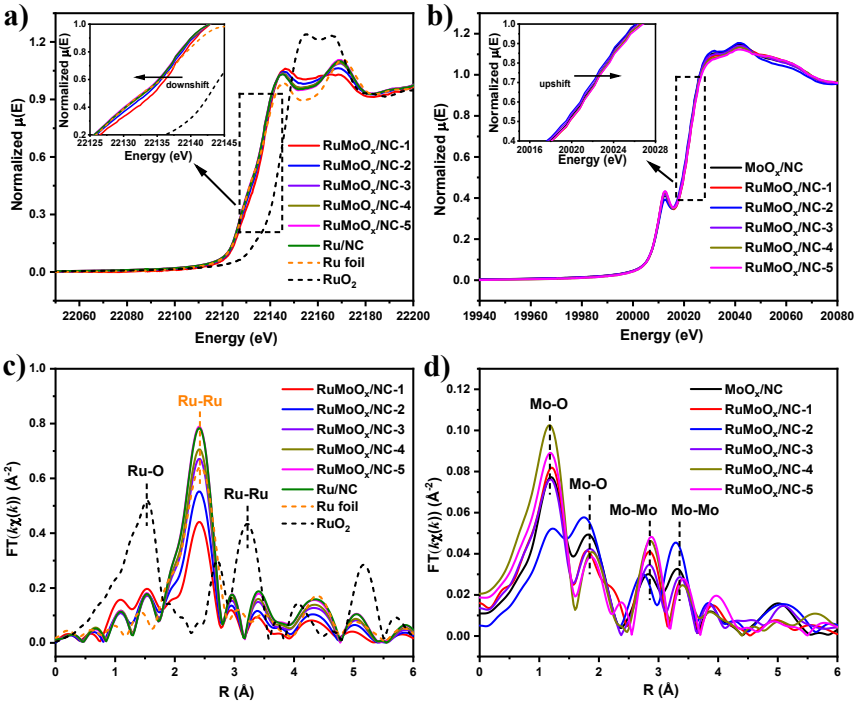

Figure 4. (a) Ru K-edge and (b) Mo K-edge XANES spectra. (c) Fourier transforms of the Ru EXAFS spectra of the sample series, Ru foil, and commercial RuO_2. (d) Fourier transforms of the Mo EXAFS spectra of the sample series.

Consistent results were obtained in X-ray absorption spectroscopy (XAS) measurements. **Figure 4a** shows the Ru K-edge X-ray absorption near-edge structure (XANES) spectra. One can see that the edge energy of the sample series was similar to that of Ru foil, suggesting a valence state close to 0, in accordance with results from the above TEM and XPS measurements where metallic Ru was the dominant component. Moreover, the absorption edge can be seen to shift to a slightly higher energy from $RuMoO_x$/NC-5 to $RuMoO_x$/NC-1 (**Figure 4a** inset), consistent with the blue shift of the Ru 3p binding energy, as observed in XPS measurements (**Figure 3d**). The corresponding Mo K-edge XANES spectra are displayed in **Figure 4b** and inset, where an opposite trend was observed with the absorption edge energy, also in good agreement with results from XPS measurements (**Figure 3e**). In addition, all samples can be seen to exhibit a pre-edge peak at ca. 20013 eV due to the dipole-forbidden 1s to 4d transition into the π* orbitals along the Mo-O bond vector, and the fact that the peak amplitude increased from $RuMoO_x$/NC-1 to $RuMoO_x$/NC-5 (**Figure S17**) suggests a diminishing amount of oxygen vacancies and hence an increasing valence state of Mo.[41] This is in excellent agreement with results from EPR (**Figure 3b**) and XPS measurements (**Figure 3d**).

Figure 4c-d show the corresponding Fourier transforms of the extended X-ray absorption fine structure (FT-EXAFS) spectra. One can see from **Figure 4c** that the Ru K-edge EXAFS spectra of the nanocomposites closely resembled that of Ru foil, featuring a main peak at ca. 2.42 Å due to the Ru-Ru path.[42] Note that the peaks of Ru-O and Ru-Ru in RuO_2 are situated at ca. 1.54 Å and 3.21 Å, and no such features can be detected in the nanocomposites, suggesting the absence of RuO_x species.[43] The Mo K-edge FT-EXAFS spectra are shown in **Figure 4d,** where the nanocomposites can be seen to possess four peaks. The dominant peak at ca. 1.19 Å most likely arose from the Mo-O first-shell path, the second at ca.1.85 Å due to the contribution of the Mo-O second shell, and the remaining two at ca. 2.86 Å and 3.36 Å to the Mo-Mo paths of MoO_3.[44-46] Taken together, these results are consistent with the formation of Ru nanoparticles supported onto a MoO_3 scaffold, in good accord with the conclusion from the above TEM and XPS measurements. Note that while Ru-Cl species were readily identified in XPS measurements (**Figure 3**), the content (**Table S2**) was too low to make a meaningful impact on EXAFS fitting, such that the Ru-Cl path, which was located slightly below 2.0 Å, was not resolved. We observed a similar phenomenon in an earlier study.[10]

From fitting of the Ru and Mo K-edge FT-EXAFS spectra (**Figure S18-S19**), the coordination number (CN) of Ru-Ru in all the samples can be found to increase from 5.18 for $RuMoO_x$/NC-1 to 6.20 for $RuMoO_x$/NC-2, 7.54 for $RuMoO_x$/NC-3, 7.96 for $RuMoO_x$/NC-4, 8.88 for $RuMoO_x$/NC-5 and 8.84 for RuNC **(Table S6)**. This is consistent with the increasing Ru nanoparticle core size in the series (**Figure S7**). Concurrently, the CN for the first and third shells of Mo-O was observed to vary only slightly within the range of 1.39 to 1.69, with the second shell from 2.61 to 3.22. Additionally, the CN for the first and second shells of Mo-Mo was estimated to be in the range of 0.61 to 1.22 and 3.39 to 2.78, respectively. It should be noted that no Ru-Mo path can be resolved, likely due to the dispersion of ruthenium nanoparticles onto the MoO_x scaffold and the minimal amount of interfacial contacts.

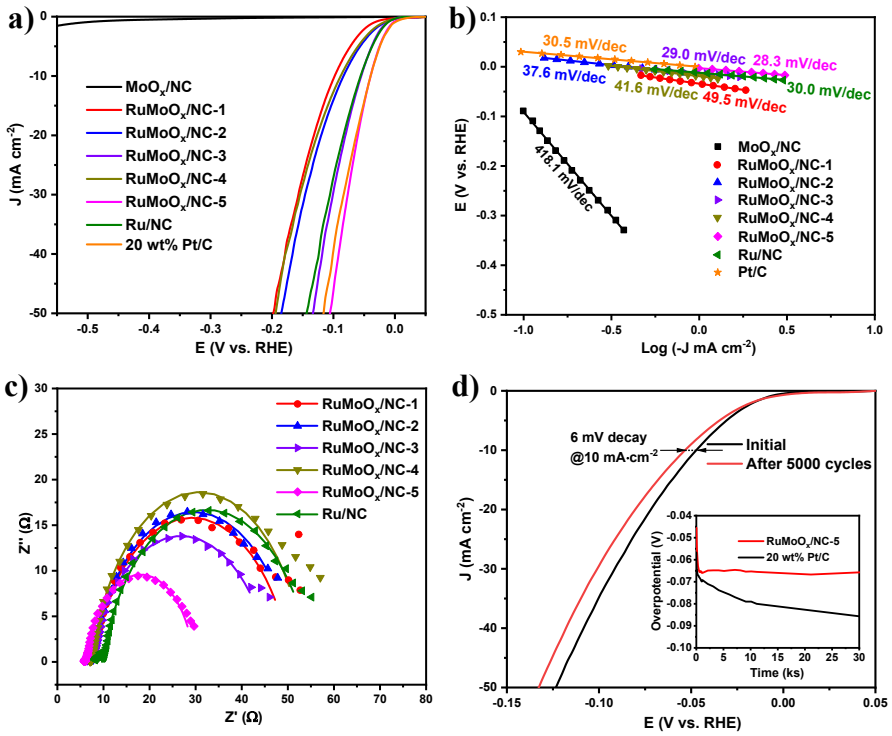

Figure 5. (a) HER polarization curves in 1 M KOH, (b) Tafel plots, and (c) Nyquist plots at the overpotential of -100 mV of the sample series in 1 M KOH. (d) HER polarization curves of RuMoO$_x$/NC-5 before and after 5000 CV cycles. Inset is the chronopotentiometric curves of RuMoO$_x$/NC-5 and 20 wt% Pt/C at the current density of 10 mA cm^{-2} for 30000 s.

Remarkably, the resulting nanocomposites display an apparent HER activity in both alkaline and acidic media. **Figure 5a** shows the HER polarization curves of the nanocomposites in 1 M KOH. One can see that NC (**Figure S20a**) and MoO$_x$/NC showed virtually no activity in alkaline media. However, markedly enhanced activity was observed with the incorporation of Ru, where η_{10} decreased significantly to -98 mV for RuMoO$_x$/NC-1, -83 mV for RuMoO$_x$/NC-2, -55 mV for RuMoO$_x$/NC-3, -89 mV for RuMoO$_x$/NC-4, -39 mV for RuMoO$_x$/NC-5, and -55 mV for Ru/NC, in comparison to -40 mV for Pt/C. That is, RuMoO$_x$/NC-5 stood out as the best HER catalysts among the series (note that at higher current densities, RuMoO$_x$/NC-5 even outperformed Pt/C), and the fact that the performance of RuMoO$_x$/NC-5 was even better than that of Ru/NC suggests that the high HER activity was facilitated by the synergistic interaction between Ru and MoO$_x$.

In fact, when the RuMoO$_x$/NC-5 nanocomposite was subject to H_3PO_4 etching, whereas the sample morphology remained mostly unchanged and Ru nanoparticles clearly resolved (**Figure S21**), XPS measurements (**Figure S22**) showed a dramatic decrease of the Mo content from 0.34 at% to 0.17 at%

whereas virtually no change for Ru (from 3.31 at% to 3.18 at%), indicating efficient removal of MoO_3 from the nanocomposite by phosphoric acid,[47] and meanwhile the content of Cl decreased sharply from 2.92 at% to 0.63 at% (**Table S2**). With the apparent losses of both Mo and Cl, the Ru 3p binding energies became increasingly similar to those of Ru/NC (**Table S4**), hence leading to a marked diminishment of the HER activity (**Figure S20b**). These results further confirmed that the high HER activity of $RuMoO_x$/NC-5 was primarily due to the electronic interactions between Ru and MoO_x, with minimal contributions from the N-doped carbon.

Figure 5b shows the Tafel plots derived from the polarization curves in **Figure 5a**, where $RuMoO_x$/NC-5 can be seen to display the lowest slope of 28.3 mV dec^{-1}, as compared to MoO_x/NC (418.1 mV dec^{-1}), $RuMoO_x$/NC-1 (49.5 mV dec^{-1}), $RuMoO_x$/NC-2 (37.6 mV dec^{-1}), $RuMoO_x$/NC-3 (29.0 mV dec^{-1}), $RuMoO_x$/NC-4 (41.6 mV dec^{-1}), Ru/NC (30.0 mV dec^{-1}), and Pt/C (30.5 mV dec^{-1}), suggesting fastest HER electron-transfer kinetics with $RuMoO_x$/NC-5. In fact, the performance of $RuMoO_x$/NC-5 is highly comparable to or even better than leading results of relevant catalysts reported recently in the literature (**Table S7)**.

Consistent results were obtained from electrochemical impedance measurements. From the Nyquist plots acquired at the overpotential of -100 mV (**Figure 5c** and **S23)**, $RuMoO_x$/NC-5 can be seen to exhibit the lowest charge-transfer resistance (R_{ct} = 14.5 Ω), as compared to $RuMoO_x$/NC-1 (21.2 Ω), $RuMoO_x$/NC-2 (23.7 Ω), $RuMoO_x$/NC-3 (20.6 Ω), $RuMoO_x$/NC-4 (21.5 Ω), and Ru/NC (24.1 Ω) (**Table S8**). In addition, one can observe that the serial resistance (R_s) diminishes from $RuMoO_x$/NC-1 to $RuMoO_x$/NC-5, suggesting increasing electrical conductivity of the materials, consistent with the increasing (decreasing) content of Ru (MoO_x) in the sample (**Table S2**).

Notably, $RuMoO_x$/NC-5 showed the largest double layer capacitance of 34.08 mF cm^{-2}, as compared to 21.23 mF cm^{-2} for MoO_x/NC, 13.84 mF cm^{-2} for $RuMoO_x$/NC-1, 11.75 mF cm^{-2} for $RuMoO_x$/NC-2, 14.17 mF cm^{-2} for $RuMoO_x$/NC-3, 19.18 mF cm^{-2} for $RuMoO_x$/NC-4, and 14.41 mF cm^{-2} for Ru/NC (**Figure S24-S25**).[48] The high electrochemically active surface area is anticipated to facilitate access to the catalytic active sites.

In addition, $RuMoO_x$/NC-5 shows remarkable durability with a decay of η_{10} by only 6 mV after 5000 cycles between -0.1 and 0 V. In fact, TEM measurements of $RuMoO_x$/NC-5 after 5000 CV cycles (**Figure S26)** showed that the dodecahedral morphology was largely unchanged, with clearly-defined lattice fringes of the (101) and (002) planes of metallic Ru, very similar to the as-produced sample (**Figure 2**).

Consistent results were obtained in XPS measurements (**Figure S27**), where metallic Ru remained the dominant species, with only a small red-shift of 0.2 – 0.3 eV for the Ru $3p_{3/2}/3p_{1/2}$ doublet binding energies (**Table S4**); and the Cl signal diminished drastically, likely because of electrochemical reduction of the residual $RuCl_x$ species into metallic Ru. In chronopotentiometric measurements (**Figure 5d inset**), virtually no decay was observed of the overpotential of $RuMoO_x$/NC-5 for 30,000 s at the current density of 10 mA cm^{-2}, in contrast to a dramatic increase with Pt/C, which further confirmed the excellent stability of $RuMoO_x$/NC-5. Certainly, for practical applications, tests at higher currents for a longer period of time are needed. This will be pursued in future study.

The electrocatalytic activity towards HER in acidic media was also tested (**Figure S28-S29**), where it can be seen that $RuMoO_x$/NC-5 again stood out among the sample series, although the performance was subpar as compared to Pt/C. We also carried out measurements to test the OER activity of $RuMoO_x$/NC-5 in 1 M KOH, and observed virtually no activity, likely because of the low RuO_x content in the sample series (**Figure 3c** and **Table S2**). In addition, the samples under study above were synthesized at 300 A for 10 s, which represented the optimal condition for sample preparation (**Figure S30-S32)**.

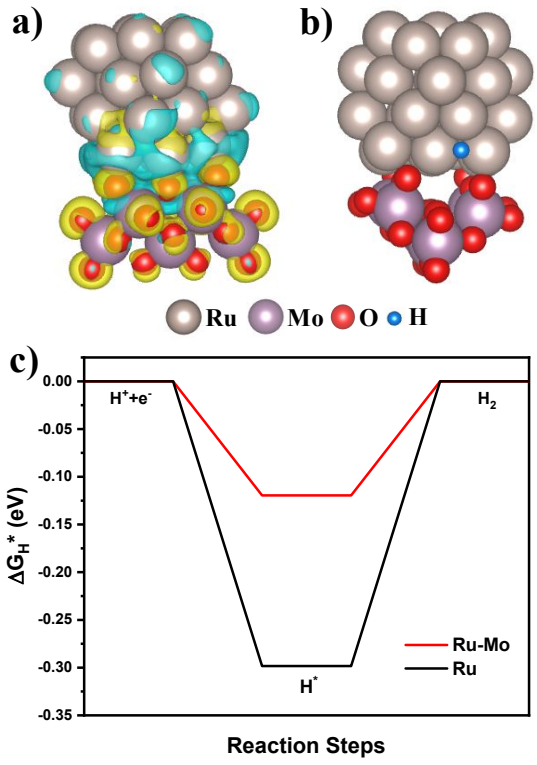

Figure 6. (a) Charge density distribution of the structural model consisting of a Ru cluster supported on a molybdenum oxide cluster. The cyan and yellow areas represent electron loss and gain, respectively. The

isovalue of charge density is 0.001 e au^{-3}. (b) H adsorption on the Ru cluster supported on a molybdenum oxide cluster. (c) Gibbs free energy of H* adsorption (ΔG_{H*}) on a Ru cluster with and without the modification of a molybdenum oxide cluster.

To unravel the mechanistic insights into the enhanced electrocatalytic activity of $RuMoO_x$/NC composites as compared to the monometal counterparts, a structural model was constructed with a Ru cluster supported onto a molybdenum oxide cluster (Ru/MoO_x), based on results from the above experimental characterizations. The electronic interactions between the Ru and MoO_x clusters is evidenced in Bader charge analysis. From **Figure 6a**, one can see a transfer of 3.2 electrons from the Ru cluster to the MoO_x cluster. This is consistent with results from the above XPS and XAS measurements (**Figure 3-4**). The resultant electron-deficient Ru is anticipated to weaken H adsorption arising, leading to an enhanced HER activity, as observed experimentally with the $RuMoO_x$/NC composites.[7, 9]

This is also manifested in the analysis of the Gibbs free energy of H* adsorption (ΔG_{H*}) onto the Ru cluster (**Figure 6b**), a commonly used descriptor of HER electrocatalysis, where a $|\Delta G_{H*}|$ close to zero eV is preferred for optimal performance.[7, 9] From **Figure 6c**, one can see that the addition of a MoO_x cluster markedly reduced the $|\Delta G_{H*}|$ on the Ru cluster to |-0.12 | eV from |-0.30 | eV for the bare Ru cluster. This is, again, consistent with the enhanced HER activity of $RuMoO_x$/NC composites observed above. Additionally, the HER activity may be facilitated by N doping that enhanced the electrical conductivity of the carbon scaffold, as manifested by the minimal serial resistance in electrochemical impedance measurements (**Figure 5c**), as well as from Cl residues that further depleted the Ru electron density by interfacial charge transfer, as demonstrated previously.[10]

Conclusion

In summary, a series of $RuMoO_x$/NC composites were prepared via a rapid MIH procedure where Ru nanoparticles were loaded onto MoO_x supported on a nitrogen-doped carbon matrix. The composites were found to exhibit a markedly enhanced HER activity in both acidic and alkaline media, as compared to the monometal counterparts. This was ascribed to electron transfer from Ru to MoO_x that weakened the H adsorption on Ru, as manifested in XPS and XAS measurements and confirmed in theoretical studies based on DFT calculations. Results from this study highlight the fundamental significance of interfacial electron transfer in manipulating the adsorption energetics of key reaction intermediates and hence the

electrocatalytic activity. Such fundamental insights can be exploited for the structural engineering of nanocomposites based on earth-abundant transition metals as high-performance electrocatalysts that can rival the precious metal-based counterparts.

Experimental Section

Chemicals. 2-Methylimidazole ($CH_3C_3H_2N_2H$, 99%, Acros Organics), zinc nitrate hexahydrate ($Zn(NO_3)_2{\cdot}6H_2O$, certified ACS, Fisher Chemicals), ruthenium(III) chloride hydrate ($RuCl_3 \cdot xH_2O$, 35-40 % Ru, Acros), ammonium molybdate tetrahydrate ($(NH_4)_6Mo_7O_{24}{\cdot}4H_2O$, certified ACS, Fisher Chemicals), potassium hydroxide (KOH, certified ACS, Fisher Chemicals), Pt/C (20 wt%, Alfa Aesar), methanol (CH_3OH, certified ACS, Fisher Chemicals), Nafion 117 solution (95%, Aldrich), 2-propanol ($(CH_3)_2CHOH$, HPLC Grade, Fisher Chemicals), sulfuric acid (H_2SO_4, 98%, Fisher Chemicals), and phosphoric acid (H_3PO_4, 65%, Sigma-Aldrich) were used as received. Deionized water was obtained via a Barnstead Nanopure water system (18.3 MΩ cm).

Synthesis of ZIF-8. ZIF-8 was synthesized by following a literature procedure.[49] Typically, 1.190 g of $Zn(NO_3)_2{\cdot}6H_2O$ was dissolved in 30 mL of methanol in a flask, and 1.314 g of 2-methylimidazole was dissolved in 15 mL of methanol in another flask. The two solutions were then blended under sonication for 15 min to produce a milky-white solution, which was transferred into a 100 mL Teflon-lined stainless-steel autoclave and heated at 120 °C for 4 h. The milky sediment was collected by centrifugation at 6000 rpm for 5 min, rinsed three times with methanol, and dried under vacuum at 60 °C overnight, affording the ZIF-8 powders.

Synthesis of N-doped carbon. NC was prepared via controlled pyrolysis of ZIF-8. Briefly, the ZIF-8 powders prepared above were put into a ceramic boat, which was transferred into a tube furnace and calcined at 900 °C for 3 h at a heating rate of 5 °C min^{-1} under a flowing N_2 atmosphere, producing NC as black powders.

Synthesis of $RuMoO_x$/NC nanocomposites. The samples were prepared by using a MIH procedure reported previously.[10, 19-21] In brief, 25 mg of the N-doped carbon prepared above was dispersed under sonication for 30 min in 2 mL of a solution containing a varied amount of $RuCl_3$ and $(NH_4)_6Mo_7O_{24}$ at the Mo:Ru molar ratios of 4:1, 2:1, 1:1, 1:2 and 1:4 with the total metal content kept roughly constant at 20 wt% of the carbon scaffold. The resultant solutions were freeze-dried to produce a black powder, which was deposited onto an iron sheet (2.5 cm × 2.5 cm × 0.2 mm) covered with a piece of graphite paper (0.01 mm in thickness, which was used to isolate the samples from the iron sheet and minimize contamination). The assembly was

placed in the center of a firebrick within a quartz tube, which was purged with an Ar gas for 10 min before being put into a four-turn induction coil (5 cm in diameter). MIH treatment was carried out at the current of 300 A for 10 s. The resulting samples were denoted as $RuMoO_x$/NC-n (n = 1, 2, 3, 4, and 5). Monometal MoO_x/NC and Ru/NC were synthesized in the same fashion but without the addition of $RuCl_3$ or $(NH_4)_6Mo_7O_{24}$ before freeze-drying, respectively.

Acid etching experiment was conducted by dispersing 30 mg of the $RuMoO_x$/NC samples into 50 mL of 4 M H_3PO_4 under reflexing at 80 °C for 1 h to remove MoO_x.[47] The etched samples were collected after water rinsing for three times and dried in vacuum at 80 °C for 24 h.

Characterization. SEM and EDS studies were conducted with an Apreo SEM microscope. TEM images were acquired with a Tecnai G2 operated at 200 kV. XPS data were obtained with a Thermo Fisher K-alpha system with the binding energy calibrated against the C 1s electrons. Nitrogen sorption isotherms were acquired with a Micromeritics Tristar 3020 Porosimeter system at 77.3 K. XAS measurements were conducted at 10 K at beamline 4-1 of the Stanford Synchrotron Radiation Lightsource using an Oxford liquid helium cryostat. In EPR measurements, the prepared samples were tapped into a capillary tube and placed in the cavity resonator. Spectra were collected at room temperature with a Bruker EMX EPR spectrometer operated at the X-band frequency (~9.86 GHz) using an ER 4122SHQE resonator (Bruker). The spectra intensity was normalized by the sample mass.

Electrochemical Measurements. Electrochemical measurements were conducted with a CHI 710 electrochemical workstation in a three-electrode configuration, using a Hg/HgO (in alkaline media) or Ag/AgCl (in acidic media) reference electrode, a graphite rod counter electrode, and a glassy carbon rotating disk working electrode (surface area 0.196 cm^2). The reference electrode was calibrated against a reversible hydrogen electrode (RHE) and all the potentials in this research were referenced to the RHE. The catalyst inks were prepared by dispersing 2 mg of the samples prepared above into a mixed solution containing 740 μL of isopropanol, 250 μL of H_2O and 10 μL of Nafion under sonication for 30 min. Then 20 μL of the inks was dropcast onto the glassy carbon disk electrode surface, and dried naturally at room temperature before being coated with 5 μL of 20 wt% Nafion. The catalyst loading was 0.204 mg cm^{-2}. The HER polarization

curves were collected in 1 M KOH at the scan rate of 10 mV s^{-1} and rotation rate of 1600 rpm with 80% *iR* compensation. Electrochemical impedance spectroscopy (EIS) measurements were carried out within the frequency range of 0.1 to 10^5 Hz at an AC amplitude of 5 mV. Chronopotentiometric measurements were conducted at the current density of 10 mA cm^{-2} for 30 000 s.

Theoretical Study. First-principles computations were carried out using Quantum ESPRESSO, an open-source plane-wave code,[50] with a model consisting of a Ru_{36} cluster placed onto a molybdenum oxide cluster. A cutoff of 40 and 240 Ry for kinetics and charge density was chosen with the ultrasoft pseudopotential.[51] The smearing parameter was set at 0.01 Ry in the Marzari-Vanderbilt smearing for all calculations.[52] For geometric relaxation, the convergence was 10^{-8} Ry of the electronic energy and 10^{-4} au for the total force. Density functional perturbation theory was performed to calculate the phonon frequency as inputs for entropy and zero point energy.[53]

ACKNOWLEDGMENT

This work was supported by the National Science Foundation (CHE-1900235 and CHE-2003685). TEM, XPS and nitrogen sorption studies were conducted as part of a user project at the National Center for Electron Microscopy and Molecular Foundry, Lawrence Berkeley National Laboratory, which was supported by the Office of Science, Office of Basic Energy Sciences, of the U.S. Department of Energy under Contract No. DE-AC02-05CH11231. XAS measurements were performed at the Stanford Synchrotron Radiation Lightsource (SSRL), which is supported by the U.S. Department of Energy, Office of Science, Office of Basic Energy Sciences under Contract No. DE-AC02-76SF00515. Computational studies were carried out using the UCSC Lux supercomputer which was funded by the NSF MRI program (AST1828315).

Reference

1. Z. K. Peng, H. Y. Wang, L. L. Zhou, Y. B. Wang, J. Gao, G. J. Liu, S. A. T. Redfern, X. L. Feng, S. Y. Lu, B. J. Li and Z. Y. Liu, *J. Mater. Chem. A*, 2019, **7**, 6676-6685.
2. C. C. Lv, Z. P. Huang, Q. P. Yang, G. F. Wei, Z. F. Chen, M. G. Humphrey and C. Zhang, *J. Mater. Chem. A*, 2017, **5**, 22805-22812.

3. F. Nichols, Q. M. Liu, J. Sandhu, Z. Azhar, R. Cazares, R. Mercado, F. Bridges and S. W. Chen, *J Mater Chem A*, 2022, **10**, 5962-5970.

4. H. Y. Jin, S. Sultan, M. Ha, J. N. Tiwari, M. G. Kim and K. S. Kim, *Adv. Funct. Mater.*, 2020, **30**, 2000531.

5. T. Ding, Z. Y. Wang, L. Zhang, C. D. Wang, Y. Sun and Q. Yang, *J. Mater. Chem. A*, 2016, **4**, 15309-15315.

6. J. Zhang, T. Wang, P. Liu, Z. Q. Liao, S. H. Liu, X. D. Zhuang, M. W. Chen, E. Zschech and X. L. Feng, *Nat. Commun.*, 2017, **8**, 15437.

7. B. Z. Lu, L. Guo, F. Wu, Y. Peng, J. E. Lu, T. J. Smart, N. Wang, Y. Z. Finfrock, D. Morris, P. Zhang, N. Li, P. Gao, Y. Ping and S. W. Chen, *Nat. Commun.*, 2019, **10**, 631.

8. J. Mahmood, F. Li, S. M. Jung, M. S. Okyay, I. Ahmad, S. J. Kim, N. Park, H. Y. Jeong and J. B. Baek, *Nat. Nanotechnol.*, 2017, **12**, 441-446.

9. Y. J. Yang, Y. H. Yu, J. Li, Q. R. Chen, Y. L. Du, P. Rao, R. S. Li, C. M. Jia, Z. Y. Kang, P. L. Deng, Y. J. Shen and X. L. Tian, *Nano-Micro Lett*, 2021, **13**, 160.

10. Q. M. Liu, B. Z. Lu, F. Nichols, J. Ko, R. Mercado, F. Bridges and S. W. Chen, *SusMat*, 2022, **2**, 335-346.

11. Q. M. Liu, H. B. Zhou, F. Nichols, H. L. Kuo, R. Mercado, B. Z. Lu, W. Y. Zhu, Y. S. Liu, J. Q. Lu, F. Bridges and S. W. Chen, *Mater Adv*, 2022, **3**, 4556-4565.

12. T. He, Y. Peng, Q. X. Jia, J. E. Lu, Q. M. Liu, R. Mercado, Y. Chen, F. Nichols, Y. Zhang and S. W. Chen, *Acs Appl. Mater. Interfaces*, 2019, **11**, 46912-46919.

13. Y. C. Pi, Z. M. Qiu, Y. Sun, H. Ishii, Y. F. Liao, X. Y. Zhang, H. Y. Chen and H. Pang, *Adv Sci*, 2023, **10**, 202206096

14. J. X. Guo, D. Y. Yan, K. W. Qiu, C. Mu, D. Jiao, J. Mao, H. Wang and T. Ling, *J Energy Chem*, 2019, **37**, 143-147.

15. W. Naseeb, Q. Liu, F. Nichols, D. Pan, M. K. Khosa and S. Chen, *J. Electroanal. Chem.*, 2023, **932**, 117272.

16. S. L. Liu, C. Chen, Y. F. Zhang, Q. H. Zheng, S. D. Zhang, X. Q. Mu, C. Y. Chen, J. M. Ma and S. C. Mu, *J. Mater. Chem. A*, 2019, **7**, 14466-14472.

17. Y. Yuan, W. Han, C. C. Zhang, Q. Sun, Y. X. Hao, J. M. Zhao, J. S. Zhao, X. J. Zhong and N. Q. Zhang, *Nano Res*, 2022, **16**, 2230-2235.

18. Q. M. Liu and S. W. Chen, *Trends Chem*, 2022, **4**, 918-934.

19. B. Lu, Q. Liu, C. Wang, Z. Masood, D. J. Morris, F. Nichols, R. Mercado, P. Zhang, Q. Ge, H. L. Xin and S. Chen, *Research*, *2022*, **2022**, 9756983.

20. Q. Liu, S. McNair, F. Nichols, B. Lu, B. Yu, D. Pan, J. Ko, A. Bhuller, F. Bridges and S. Chen, *Adv. Sens. Energy Mater.*, 2023, **2**, 100046.

21. Q. M. Liu, F. Nichols, A. Bhuller, K. Singewald, H. L. Kuo, J. Q. Lu, G. L. Millhauser, F. Bridges, Q. F. Ge and S. W. Chen, *Appl Catal B: Environ*, 2024, **342**, 123399.

22. L. H. Zhu, S. Y. Shan, V. Petkov, W. W. Hu, A. Kroner, J. B. Zheng, C. L. Yu, N. W. Zhang, Y. H. Li, R. Luque, C. J. Zhong, H. Q. Ye, Z. Q. Yang and B. H. Chen, *J. Mater. Chem. A*, 2017, **5**, 7869-7875.

23. H. X. Yao, X. K. Wang, K. Li, C. Li, C. H. Zhang, J. Zhou, Z. W. Cao, H. L. Wang, M. Gu, M. H. Huang and H. Q. Jiang, *Appl Catal B: Environ*, 2022, **312**, 121378.

24. A. N. P. Raj, T. Adinaveen, R. B. Bennie, C. Joel, S. H. Kengaram and P. L. Sophie, *J Inorg Organomet P*, 2022, **32**, 4284-4294.

25. Y. X. Sun, J. Wang, B. T. Zhao, R. Cai, R. Ran and Z. P. Shao, *J. Mater. Chem. A*, 2013, **1**, 4736-4746.

26. K. S. W. Sing, D. H. Everett, R. A. W. Haul, L. Moscou, R. A. Pierotti, J. Rouquerol and T. Siemieniewska, *Pure Appl Chem*, 1985, **57**, 603-619.

27. B. Z. Yu, J. Diniz, K. Lofgren, Q. M. Liu, R. Mercado, F. Nichols, S. R. J. Oliver and S. W. Chen, *ACS Sustain. Chem. Eng.*, 2022, **10**, 15501-15507.

28. J. P. Guo, J. Wang, Z. X. Wu, W. Lei, J. Zhu, K. D. Xia and D. L. Wang, *J. Mater. Chem. A*, 2017, **5**, 4879-4885.

29. J. Wojciechowska, E. Gitzhofer, J. Grams, A. M. Ruppert and N. Keller, *Materials*, 2018, **11**, 2329.

30. M. K. Jo, H. Heo, J. H. Lee, S. Choi, A. Kim, H. B. Jeong, H. Y. Jeong, J. M. Yuk, D. Eom, J. Jahng, E. S. Lee, I. Y. Jung, S. R. Cho, J. Kim, S. Cho, K. Kang and S. Song, *Acs Nano*, 2021, **15**, 18113-18124.

31. B. Yan, Y. Y. Liu, Y. L. Zhang, Y. J. Guo, W. Guo, L. Chen, F. Yu and G. Wang, *Mater Lett*, 2020, **273**, 127861.

32. Z. Y. Tang, G. H. Zhang, H. Zhang, L. Wang, H. M. Shi, D. H. Wei and H. G. Duan, *Energy Storage Mater*, 2018, **10**, 75-84.

33. X. H. Zhang, X. Chen, C. G. Chen, T. Liu, M. M. Liu, C. C. Zhang, T. Huang and A. S. Yu, *RSC Adv.*, 2018, **8**, 39829-39836.

34. E. Lee, T. H. Kim, S. W. Lee, J. H. Kim, J. Kim, T. G. Jeong, J. H. Ahn and B. Cho, *Nano Converg*, 2019, **6**, 24.

35. A. Yu, Y. Zhao, L. Zhu, W. Yang, P. Peng and F.-F. Li, *Chem Eng J*, 2023, **462**, 142268.

36. B. Z. Lu, B. Yao, G. Roseman, C. P. Deming, J. E. Lu, G. L. Millhauser, Y. Li and S. W. Chen,

Chemelectrochem, 2017, **4**, 2211-2217.

37. J. W. Zhang and C. Q. Teng, *Mater Design*, 2020, **192**, 108774.
38. D. Escalera-Lopez, Y. B. Niu, S. J. Park, M. Isaacs, K. Wilson, R. E. Palmer and N. V. Rees, *Appl Catal B-Environ*, 2018, **235**, 84-91.
39. W. X. Ji, R. Shen, R. Yang, G. Y. Yu, X. F. Guo, L. M. Peng and W. P. Ding, *J. Mater. Chem. A*, 2014, **2**, 699-704.
40. B. Z. Yu, Q. M. Liu, F. Nichols, K. Mayford, D. J. Pan, H. L. Kuo, J. Q. Lu, F. Bridges and S. W. Chen, *J. Phys. Chem. C* . 2023, **127**, 3996-4005.
41. S. Reschke, K. G. V. Sigfridsson, P. Kaufmann, N. Leidel, S. Horn, K. Gast, C. Schulzke, M. Haumann and S. Leimkuhler, *J Biol Chem*, 2013, **288**, 29736-29745.
42. Y. C. Lin, Z. Q. Tian, L. J. Zhang, J. Y. Ma, Z. Jiang, B. J. Deibert, R. X. Ge and L. Chen, *Nat. Commun.*, 2019, **10**, 162.
43. J. L. Cai, J. Ding, D. H. Wei, X. Xie, B. J. Li, S. Y. Lu, J. M. Zhang, Y. S. Liu, Q. Cai and S. Q. Zang, *Adv. Energy Mater.*, 2021, **11**, 2100141.
44. W. Y. Qu, X. N. Liu, J. X. Chen, Y. Y. Dong, X. F. Tang and Y. X. Chen, *Nat. Commun.*, 2020, **11**, 1532.
45. D. Han, S. Hwang, S. M. Bak and K. W. Nam, *Electrochim Acta*, 2021, **388**, 138635.
46. S. Borg, W. H. Liu, B. Etschmann, Y. Tian and J. Brugger, *Geochim Cosmochim Acta*, 2012, **92**, 292-307.
47. P. Cannon, *J Inorg Nucl Chem*, 1959, **11**, 124-127.
48. Y. Peng, W. Z. Pan, N. Wang, J. E. Lu and S. W. Chen, *ChemSusChem*, 2018, **11**, 130-136.
49. Q. M. Liu, Y. Peng, Q. X. Li, T. He, D. Morris, F. Nichols, R. Mercado, P. Zhang and S. W. Chen,

Acs Appl. Mater. Interfaces, 2020, **12**, 17641-17650.

50. P. Giannozzi, S. Baroni, N. Bonini, M. Calandra, R. Car, C. Cavazzoni, D. Ceresoli, G. L. Chiarotti, M. Cococcioni, I. Dabo, A. Dal Corso, S. de Gironcoli, S. Fabris, G. Fratesi, R. Gebauer, U. Gerstmann, C. Gougoussis, A. Kokalj, M. Lazzeri, L. Martin-Samos, N. Marzari, F. Mauri, R. Mazzarello, S. Paolini, A. Pasquarello, L. Paulatto, C. Sbraccia, S. Scandolo, G. Sclauzero, A. P. Seitsonen, A. Smogunov, P. Umari and R. M. Wentzcovitch, *J Phys: Condens Mat*, 2009, **21**, 395502.
51. K. F. Garrity, J. W. Bennett, K. M. Rabe and D. Vanderbilt, *Comput. Mater. Sci.*, 2014, **81**, 446-452.
52. Y. Peng, Q. M. Liu, B. Z. Lu, T. He, F. Nichols, X. Hu, T. Huang, G. Huang, L. Guzman, Y. Ping and S. W. Chen, *Acs Catal*, 2021, **11**, 1179-1188.
53. S. Baroni, S. de Gironcoli, A. Dal Corso and P. Giannozzi, *Rev Mod Phys*, 2001, **73**, 515-562.